An Inductively Coupled Plasma System for Investigating Spectropolarimetric Responses of Solar Plasmas to Anisotropic Fields

Tomoko KAWATE[1,2], Haruhisa NAKANO[1,2], Yuwei HUANG[3], Daiki YAMASAKI[3,4], Kiyoshi ICHIMOTO[3], Motoshi GOTO[1,2], Satoru UENO[3], Goichi KIMURA[3], Joseph J. SIMONS[2] and Yasuko KAWAMOTO[1]

[1]*National Institute for Fusion Science, Toki 509-5292, Japan*
[2]*The Graduate University for Advanced Studies, SOKENDAI, Toki 509-5292, Japan*
[3]*Kyoto University, Kyoto 606-8502, Japan*
[4]*Institute of Space and Astronautical Science, Japan Aerospace Exploration Agency, Sagamihara 252-5210, Japan*

(Received 6 February 2023 / Accepted 5 April 2023)

High precision measurements and accurate modeling of atomic polarization under three-dimensional radiation transfer are crucial to understand the structures of magnetized solar plasmas. To develop and validate spectropolarimetric measurements and analyses, we set up an inductively coupled plasma (ICP) generator designed especially for ∼1-eV plasmas interacting with radiation and weak magnetic fields. The device was put in front of the focal plane of the Horizontal Spectrograph of the Domeless Solar Telescope at Hida Observatory of Kyoto University. In helium discharges, the typical electron temperature, electron density, and helium column density of the ICP are comparable values to those of solar prominences, and the direct comparison of spectra shows almost the same opacity at He I 1083 nm. Magnetic and radiation fields were introduced to the ICP, and the system successfully reproduced reasonable spectropolarimetric signals as compared with those from the solar prominences.

Keywords: astrophysical plasma, spectroscopy, polarization, diagnostics

DOI: 10.1585/pfr.18.1401037

1. Introduction

A magnetic field is a fundamental physical quantity for the structural formation of plasmas. One of the popular techniques to measure a magnetic field in plasmas is the spectropolarimetry of atomic/ionic emission lines. In solar/stellar observations, polarimetric measurements have been made to derive the magnetic field [1], whereas in magnetically confined fusion plasmas, the spatial distribution of an atomic/ionic population has been examined under given magnetic fields [2]. On the other hand, under the three dimensional radiation transfer problem, atomic/ionic populations are affected by anisotropic radiation from the non-local population density in the plasma. In addition to solar plasmas, the method to derive magnetic fields is limited to passive spectroscopy, although measurements of as weak a magnetic field as $\lesssim 1$ mT (10 G) is needed. Thus, high precision measurements as well as accurate modeling of atomic polarization under three-dimensional radiation transfer are crucial for understanding the structures of magnetized solar plasmas.

Solar prominence, or dark filament if it is observed on the solar disk, is one of the attractive phenomena for which formation and evolution have been intensively discussed from the view point of magnetic field structures. Prominence is a cool (∼1 eV) and dense (∼ 10^{17} m^{-3}) plasma floating in the hot (∼100 eV) and dilute (∼ 10^{15} m^{-3}) corona [3, 4]. How these cool plasmas are confined and sustained in the hot corona against the gravity force has been roughly understood as they are sustained in magnetic dips aligned above magnetic polarity inversion lines in the photosphere. However, how these magnetic dips are formed, catch particles, and sometimes erupt into interplanetary space is a long-standing problem. Many models have been proposed [5, 6], and precise spectropolarimetric measurements have been performed [7, 8] to validate the models. On the other hand, prominences are intrinsically irradiated by the bright solar photosphere, and external and internal anisotropic radiation fields to the prominence plasmas create a population imbalance and quantum coherence among magnetic sublevels [9]. These atomic processes make it difficult to interpret the observed spectropolarimetric signals in simple ways.

To develop and validate measurements and analyses of a complex plasma system, a popular way is setting up a test plasma with the same plasma parameters and/or configuration but a simpler system. In this study, we set up

author's e-mail: kawate.tomoko@nifs.ac.jp

an inductively coupled plasma (ICP) designed especially for spectropolarimetric measurements of plasmas interacting with radiation and weak magnetic fields, and observed the laboratory plasma by using a spectropolarimetric system designed and operated for solar observations. The paper reports on the experimental system and some examples of observed spectropolarimetric signals aiming at the understanding of the magnetic structures of solar plasmas. Section 2 introduces an experimental system for investigating anisotropic radiation and magnetic fields. Section 3 presents examples of the obtained spectropolarimetric signals . Finally Sec. 4 summarizes the paper.

2. Experimental Setup

We performed experiments by setting an ICP device in front of the focal plane of the Horizontal Spectrograph of the Domeless Solar Telescope [10] at Hida Observatory of Kyoto University. In the spectrograph, a spectropolarimeter [11] with high spectral resolution and high polarimetric sensitivity is installed. This system allowed us to compare weak polarization signals from ICP and solar plasmas directly.

Figure 1 shows a schematic drawing of the experimental setup of the ICP. The device consists of a quartz pipe coupling an antenna and of a vacuum chamber made of stainless steel. The radio-frequency (RF) antenna was made of a copper tube and formed in a 6.5-turn coil. An RF power of 13.56 MHz was applied to the antenna through an automatic impedance matching network (ASTECH TH-50SR) using an RF power generator (Advanced Energy Cesar 1350). The base pressure was maintained at about 10^{-3} Pa using a rotary pump (RP) and a turbo-molecular pump (TMP). In this study, helium gas was introduced into the chamber and the flow rate was controlled by a mass flow controller (MFC). The He pressure was monitored by a pressure gauge (VISTA CC-10). The typical flow rate for 5.0 Pa was 117 standard cubic centimeters per minute. By controlling RF powers and neutral gas pressures, we could change the electron temperature and electron density of the ICP. We defined the z-axis as the vertical direction, i.e. the axis of the RF antenna, and the x-axis as the line-of-sight (LoS) direction through the center of the slit of the spectrometer, as shown in Fig. 1. We set viewports made of fused silica on the four sides of the vacuum chamber in the xy-plane, and spectroscopic measurements were done through a viewport on the x-axis. The size of each viewport was ϕ63 mm. By using light sources and magnets, we could apply external radiations and magnetic fields to the ICP on the xy-plane at the same time. The x-axis was also on the light path from the solar telescope, and we could perform experiments of photo-absorption by the ICP with the background solar radiations.

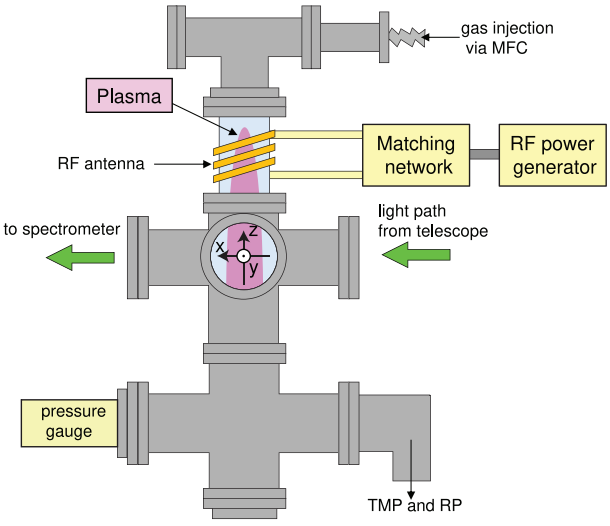

Fig. 1 Apparatus for plasma experiments. z-axis shows vertical direction, whereas x-axis shows direction along line of sight of spectrometer.

Here we focus on helium spectra, especially at He I 1083 nm that correspond to the transition between $1s2s\,^3\mathrm{S}$ and $1s2p\,^3\mathrm{P}$. Helium is the second most abundant element in the sun, and, due to its relatively simple atomic structure, the spectra have been intensively investigated in both astrophysical and laboratory plasmas. The metastable state of triplet, $1s2s\,^3\mathrm{S}_1$, has characteristics of relatively high excitation energy (19.8 eV) and a long lifetime ($\sim$ 8000 sec) [12]. These characteristics affect the validity of diagnostics under quasi-steady state approximations [13], energy transport [14], penning ionization [15], and thus plasma processing [16]. In solar plasmas, He triplet transitions have been examined for plasma diagnostics as well as their formation mechanism [17]. Hence, modeling and validation of the helium spectra have been performed in many plasma-related fields [18–22], and they are a good target to demonstrate the new experimental system. The transition wavelengths of $2^3\mathrm{S}_1$–$2^3\mathrm{P}_0$, $2^3\mathrm{S}_1$–$2^3\mathrm{P}_1$, and $2^3\mathrm{S}_1$–$2^3\mathrm{P}_2$ are 1082.909, 1083.025, and 1083.034 nm, respectively. Hereafter we denotes these wavelengths as λ_{10}, λ_{11}, and λ_{12}, respectively. The emission/absorption lines at λ_{11} and λ_{12} are blended in solar observations. We call the line at λ_{10} "blue component" and the line at λ_{11} and λ_{12} "red component".

The Horizontal Spectrograph [10] is a Czerny-Turner type spectrometer with a focal length of 10 m. It is equipped with three gratings, and we used the 600-line mm^{-1} grating in this study. The optical configuration of the spectrometer is described in Fig. 12 of Ref. [10]. The spectropolarimeter [11] consists of a super achromatic waveplate mounted in a rotating mechanism and a polarizing beam splitter assembly. These are mounted just behind the entrance slit of the spectrograph, and the waveplate has nearly constant retardation of about 127° over a wavelength range of 500 - 1100 nm. The polarization analyzer is an assembly of five beam-splitter cubes, and the two beams exiting from the polarization analyzer are linearly polarized in the directions of ±45° with respect to the slit. By

Table 1 Comparison of typical plasma parameters between ICP and solar prominence.

params	ICP	solar prominence
system size L [m]	0.2	10^{7}
Gas pressure [Pa]	0.4 - 30	$10^{(-4)-(-2)}$
T_e [eV]	1 - 10	~1
T_{He} [eV]	<0.1	~1
N_e [m^{-3}]	10^{15-17}	10^{15-17}
N_{He} [m^{-3}]	10^{19-21}	10^{13-16}
$N_{He}L$ [m^{-2}]	10^{18-20}	10^{20-23}

using this system, we obtained full Stokes parameters I_{total}, $Q = I_{0^\circ} - I_{90^\circ}$, $U = I_{45^\circ} - I_{135^\circ}$, $V = I_r - I_l$, where I_{total} is the total intensity, I_θ is the linearly polarized intensity along the direction of θ degrees from the y-axis on the yz-plane, and $I_{r(l)}$ is the right (left)-circularly polarized intensity, at each wavelength. This system demonstrates superior performance over the wavelength range of 500 - 1100 nm. As a detector, we used a near infrared camera (Allied Vision Technologies Goldeye G033 SWIR). The pixel size, the number of pixels, and the full frame rate of the camera are 15×15 μm^2, 640×512 pixels^2, and 301 frames sec^{-1}, respectively. We put a 0.23-times demagnification optical system between the exit of the spectrometer and the camera, and the spectral sampling was 3.90 pm. With this system, high polarization sensitivity of $\sim 3 \times 10^{-4}$ is achieved within a few seconds for solar observations.

The comparison of plasma parameters between the ICP [23] and solar prominence [24] is shown in Table 1. Although their system sizes, L, differ by eight orders of magnitude, the electron temperatures ,T_e, the electron densities, N_e, and the column densities of He atoms, $N_{He}L$ where N_{He} is the He atomic density, are comparable between these plasmas. Therefore, we can study responses to plasma parameters and anisotropic fields between the laboratory and solar plasmas by the same measurement system.

3. Examples of Obtained Spectra

In this section, we show three examples of obtained spectra from the viewpoint of intensity profiles of ICP and solar prominence spectra, polarization responses to magnetic fields, and those to radiation fields.

3.1 Comparison with solar prominence spectra

First, we compare spectra observed from ICP and solar prominence to confirm the similarities and differences. Figure 2 shows a direct comparison of the spectra from the ICP and a solar prominence. The prominence observation was made on 4th September 2022, and the location of the prominence was on the east limb. To identify the telescope pointing and slit position on the solar image, we took slit-jaw images as shown in Fig. 2 (a). These were taken by a universal tunable filter [25,26] whose wavelength was centered at Hα 656.28 nm and the pass band was 25 pm. The image on the slit was focused again at the detector, and the spatial sampling of the spectrogram was 0.41 arcsec pix^{-1}, which corresponds to 300 km pix^{-1} on the sun. The slit width was 20 μm, where the corresponding spectral width at 1083 nm was 1.21 pm.

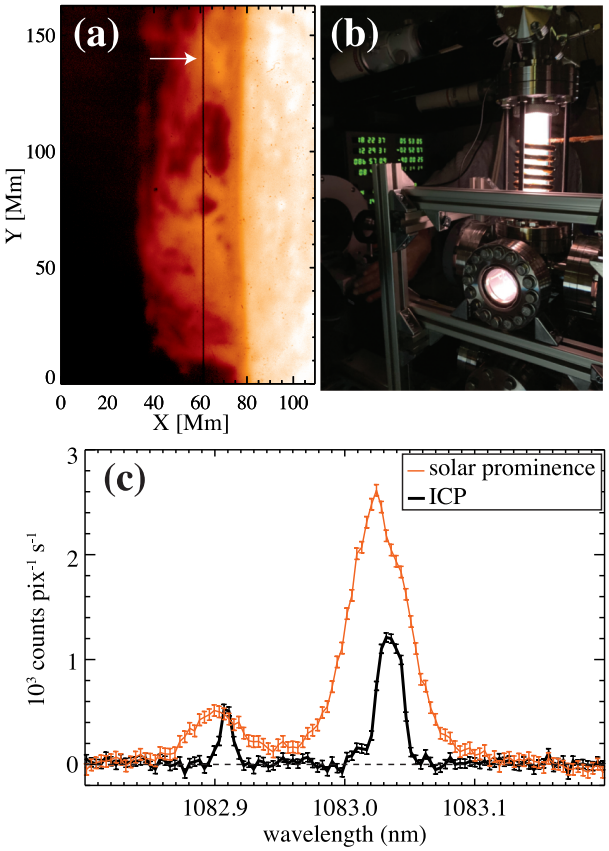

Fig. 2 (a) Slit-jaw Hα image of solar prominence. Vertical black line shows slit of spectrometer, and white arrow shows position at which we picked up spectrum in (c). (b) Picture of ICP. (c) Observed spectra from ICP (thick black) and solar prominence (thin red) at He I 1083 nm.

The measured spectra of the prominence and ICP are shown in Fig. 2 (c) with red and black curves, respectively. Here the heating power and neutral pressure of the ICP were 50 W and 5.0 Pa, respectively, and the picture of the ICP is also presented in Fig. 2 (b). Both prominence and ICP were measured under the same conditions with an exposure time and slit width of 50 ms and 100 μm, respectively. The results show that the irradiances from both plasmas were comparable.

We perform fitting by double Gaussian functions for the ICP and prominence spectra, and derive intensity ratio between blue and red components, Doppler shift, and line width. Here the intensity of each component is calculated by integrating the best-fit Gaussian component along the wavelength. The intensity ratio between blue and red

components is known as a diagnostics of optical thickness, τ, at the emission lines. The obtained intensity ratios are 4.6 ± 0.2 and 4.5 ± 0.2 for the ICP and prominence plasma, respectively. Shikama et al. [22] calculated line ratios as a function of optical thickness for these lines. By referring the calculated relationship under assumption of a homogeneous plasma, the corresponding opacities at λ_{10}, λ_{11}, and λ_{12} nm are about 0.3, 0.9, and 1.5, respectively, for both the ICP and prominence plasmas. Here we use the relationship between the ratio of opacities and that of the statistical weights of the upper levels.

Regarding with the Doppler shift, the prominence spectrum is shifted by -5 ± 1 and -9.2 ± 0.3 pm for the blue and red components, respectively, compared with those of the ICP spectrum. The blueshifts of the blue and red components correspond to the LoS velocities of 1.4 ± 0.3 and $2.55\pm0.08\,\mathrm{km\,s^{-1}}$, respectively. Rotation speed of the sun is $\sim 2\,\mathrm{km\,s^{-1}}$. In addition, in small-scale structures of a quiescent prominence, Doppler velocities of $\pm$(6 - 10) $\mathrm{km\,s^{-1}}$ have been reported in Hα and Mg II lines [27]. Thus, the blueshifts in the observed spectrum are explained as rotation of the sun and the dynamics of the solar prominence.

The full width at half maximum (FWHM) of the spectral lines of the ICP are 10.8 ± 0.7 and 21.0 ± 0.5 pm for the blue and red components, respectively. Since the line width corresponding to the slit width was 1.21 pm, the result suggests that the width of the blue component is determined by the atomic temperature. By assuming that the instrumental width is same as the slit width, the estimated atomic temperature of the blue component is 0.031 ± 0.005 eV, which is comparable to the room temperature and reasonable for ICP plasmas. On the other hand, the red component consists of two lines, and the Gaussian width of the best fit FWHM corresponds to $(\lambda_{12} - \lambda_{11}) =$ 8.9 pm. Therefore, the red component shows a wider spectrum. On the other hand for the prominence spectrum, the FWHM of the spectral lines were 66 ± 2 and 55.8 ± 0.5 pm for the blue and red components, respectively. The width of the red component is 6.3 times larger than $(\lambda_{12} - \lambda_{11})$, and the line broadening is dominated by the atomic thermal velocity and microturbulence of the prominence plasma. Assuming that the line broadening is determined by the thermal velocity and the slit width, the atomic temperature of the prominence derived from the blue and red components are 1.2 ± 0.1 and 0.84 ± 0.02 eV, respectively.

In the solar plasma, Doppler velocities and FWHMs between blue and red components show discrepancies. It could be understood by the different opacities between blue/red components and by the distribution of plasma parameters along the LoS. The blue component is optically thin, and the effective line formation region is the entire region along the LoS. On the other hand in the red component, which is optically thick, the effective line formation region can be regarded as the region where the opacity from the observer is unity. If the plasmas closer to the observer have higher LoS velocities and cooler atomic temperatures than the averages over the entire structure, the Doppler velocities and FWHMs derived from the measurement could be explained.

3.2 External magnetic field

Second, we examine the polarization spectra under an external magnetic field. Under a magnetic field parallel to the line of sight, emissions from atoms are circularly polarized due to resolution of degeneracy by the Zeeman effect.

We put two permanent magnets on both sides of the vacuum vessel, and a magnetic field was introduced to the plasma along the x-axis, i.e, the direction of LoS. The shape of each magnet was a ring with outer and inner diameters of ϕ120 mm and ϕ60 mm, respectively, and a thickness of 20 mm. The surface magnetic flux density was 114 mT, and the distance between the two magnets was 219 mm. The magnetic field between two magnets was measured by a tesla meter (MOTHERTOOL MT-801). Due to the limitation of measurable regions inside the vacuum vessel by using probes, we also measured the magnetic field between the magnets without the vacuum vessel. We set the magnets with a distance of 219 mm and measured the axial magnetic field strength between the magnets. The measured magnetic fields inside and without the vacuum vessel show good agreement, as shown in Fig. 3 (a). The magnetic field strength was 6.80 mT at the center of the vacuum vessel. Note that typical magnetic field strength in solar prominences/dark filaments is about 0.1 - 10 mT [28]. In this study, the slit width was 100 μm to get a better signal to noise ratio for the polarimetric measurements.

Under the ICP conditions of 5.0 Pa and 100 W, the measured intensity I and Stokes parameter V with/without setting the magnets are shown in Fig. 3 (b). As shown in the figure, a circular polarization signal of $\sim$ 4% is detected when the external magnetic field is applied. As a quick investigation of the Zeeman effect, we calculate zero dimensional radiative reabsorption under a static external magnetic field. We calculate level energies resolved into magnetic sublevels for lower, $1s2s\ ^3\mathrm{S}$, and upper, $1s2p\ ^3\mathrm{P}$, levels by diagonalizing the time-independent Schrödinger equation under perturbation theory [29],

$$(H_0 - \boldsymbol{\mu} \cdot \boldsymbol{B}) \left|\Psi_{u(l)}\right\rangle = E_{u(l)} \left|\Psi_{u(l)}\right\rangle, \tag{1}$$

and the transition matrix elements between them, $\left|\langle\Psi_l| d_q |\Psi_u\rangle\right|^2$. Here H_0 is the unperturbed Hamiltonian, $\boldsymbol{\mu}$ is the magnetic moment of the atom, $\boldsymbol{B}$ is the magnetic field, u and l denotes upper and lower levels, respectively, $E_{u(l)}$ is the level energy, $\left|\Psi_{u(l)}\right\rangle$ is the eigenfunction of $(H_0 - \boldsymbol{\mu}\cdot\boldsymbol{B})$ resolved into magnetic sublevels, and d_q is the spherical tensor component of the electric dipole moment for $q = \pm1(\sigma), 0(\pi)$. We use the unperturbed energy levels provided by the Atomic Spectra Database of the National Institute of Standards and Technology (NIST) [12]. We

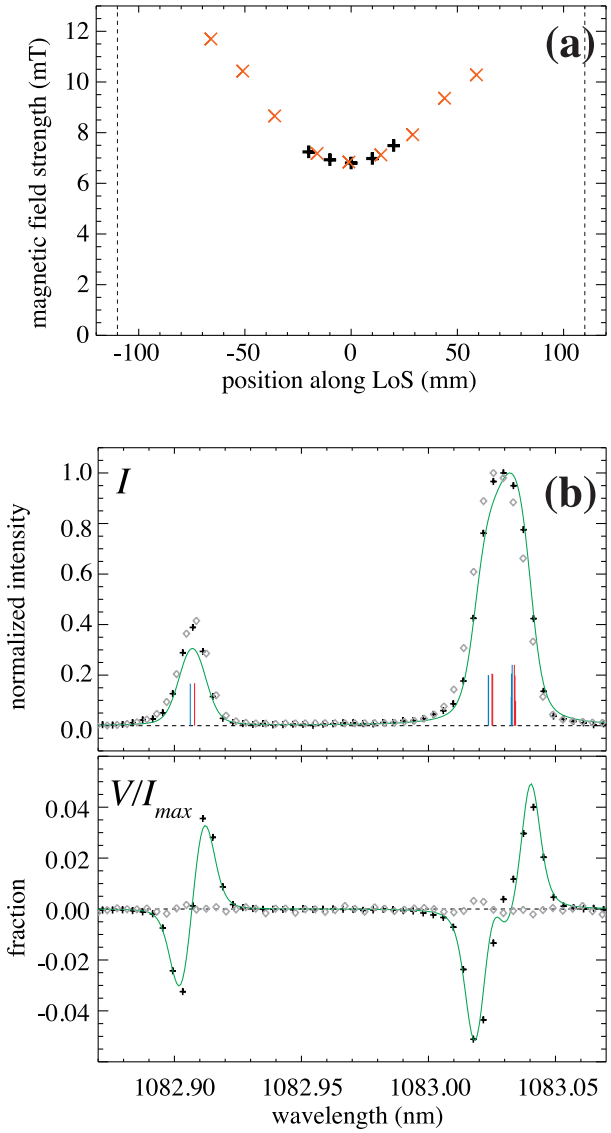

Fig. 3 (a) Measured magnetic field strength along x-axis. Black + shows magnetic field strengths measured inside vacuum vessel, whereas red × shows those measured without vacuum vessel. Vertical dotted lines show inner edge of two magnets. (b) Normalized intensity I/I_{max} and circular polarization V/I_{max} from ICP with (black +) and without (gray ◇) magnets under RF power of 100 W and neutral pressure of 5.0 Pa. Blue and red bars show intensities of $-\sigma$ and $+\sigma$ components, respectively. Green curves show best fit function.

assume a zero dimensional radiation reabsorption model [30]:

$$I_{q\nu} = \frac{\sum_i \epsilon_{i\nu}}{\sum_i \alpha_{i\nu}} \left\{ 1 - \exp\left(- \sum_i \alpha_{i\nu} L \right) \right\} , \tag{2}$$

where i is each transition between upper and lower magnetic sublevels for q, ν is the frequency of the radiation, $\epsilon_{i\nu}$ is the emissivity, $\alpha_{i\nu}$ is the absorption coefficient, and L is the plasma size along the LoS. The absorption coefficient and optical thickness are related by $\tau_\nu = \sum_i \alpha_{i\nu} L$. Thus, under an optically thin regime ($\tau_\nu \ll 1$), the intensity can be described as $I_{q\nu} \sim \sum_i \epsilon_{i\nu} L$.

The emissivity and absorption coefficient are related with the transition matrix element as

$$\epsilon_{i\nu} \propto \quad \nu n_u A_{ul} \quad \propto \nu^4 n_u \left| \langle \Psi_l | \, d_q \, | \Psi_u \rangle \right|^2 , \tag{3}$$

$$\alpha_{i\nu} \propto \quad n_l f_{lu} \quad \propto \nu n_l \left| \langle \Psi_l | \, d_q \, | \Psi_u \rangle \right|^2 , \tag{4}$$

where $n_{u(l)}$ is the population density of the upper (lower) levels, A_{ul} is the spontaneous emission coefficient, and f_{lu} is the absorption oscillator strength. We assume that the shape of each Zeeman component, $P(\lambda)$, is described by the Voigt profile:

$$P(\lambda) = \frac{\gamma}{w\sqrt{2\pi^3}} \int_{-\infty}^{\infty} \frac{\exp\left(-\frac{x^2}{2w^2}\right)}{(\lambda - \lambda_0 - x)^2 + \gamma^2} dx , \tag{5}$$

where w is the Gaussian width, γ is the Lorentzian width, and λ_0 is the wavelength at the line center. Under these assumptions, we perform a fitting of I/I_{max} and V/I_{max} profiles simultaneously by using the Levenberg-Marquardt least-squares minimization method [31–33], regarding B, w, γ, and n_l, as free parameters. The best fitting is given by $B = 8.11 \pm 0.02$ mT, $w = 4.29 \pm 0.01$ pm, $\gamma = 1.4 \pm 0.2$ pm, and $\tau_\nu = 0.291 \pm 0.007$ at λ_{10}. We plot the best fit profiles in Fig. 3 (b). Some deviations between modeled and observed spectra can be understood by the effect of spatial inhomogeneity of the plasma and/or non-gaussian instrumental line spread function.

3.3 Radiation field

Third, we examine polarization signals by photo-excitation, so-called scattering polarization. Since the spin of a photon is 1, the change of the magnetic sublevels during the transitions by photo-absorption is limited by $q = \pm 1$ with the quantization axis parallel to the photon momentum. This selective transition results in a population imbalance among the upper sublevels of $1s2s\,^3$P, and the resulting line emission is linearly polarized. In the solar atmosphere, the scattering polarization due to irradiation from the dense and bright lower atmosphere has been observed in a range from ultraviolet to infrared.

To demonstrate a polarization with a scattering of the anisotropic radiation field, we injected laser light into plasma along the y-axis in Fig. 1. We used a laser diode of Distributed Bragg Reflector (Thorlabs DBR1083PN) with an output power of 133 mW and a wavelength centered at 1083.03 nm with a pass band of 31 fm. The power and wavelength were controlled by a laser driver (Thorlabs CLD1015). The rays of the laser light were expanded and collimated to ϕ48 mm by using a quartz lens with a focal length of 200 mm and with a diameter of 50 mm. The slit width was 100 μm in this experiment.

Figure 4 shows the observed intensity, I, and Stokes parameters, Q and U, under plasma conditions of RF power of 20 W and neutral pressures of 1.5 and 5.0 Pa. By laser injection, the intensities of both blue and red components are enhanced. The enhancements of the blue and red

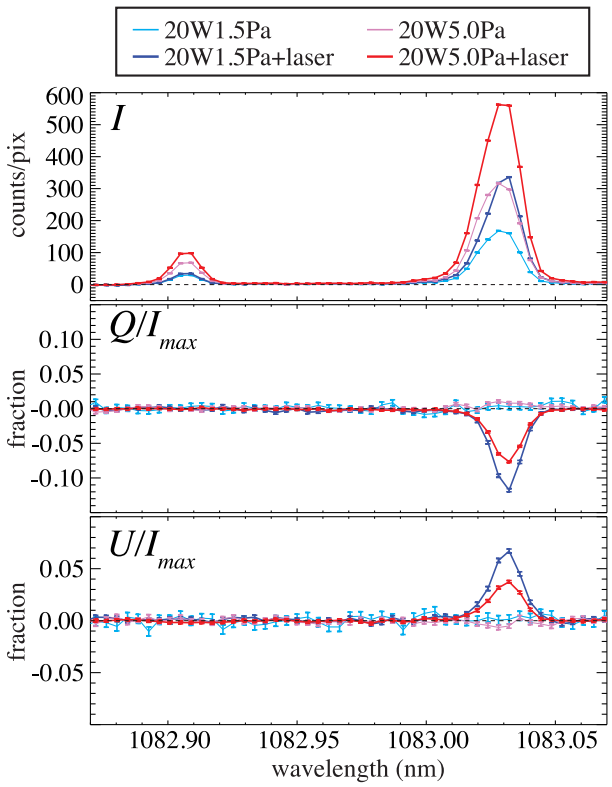

Fig. 4 Intensity I and linear polarization signals Q/I_{max}, U/I_{max} with (red, blue) and without (pink, light blue) laser injection along y-axis.

components at 1.5 Pa are 12.6±0.2% and 79.74±0.04%, respectively, whereas those at 5.0 Pa are 45.3±0.1% and 72.52±0.02%, respectively. In addition, linear polarization signals as significant as 5 - 10% appear in red components. By comparing the results with neutral pressures of 1.5 and 5.0 Pa, we can also see that higher pressure causes smaller polarization signals. This can be understood by increase of disalignment by elastic collision and/or depopulation by inelastic collision [34–36]. In the case of higher neutral pressure, i.e., higher collision rates, the anisotropic effect becomes relatively small.

4. Summary

In this study, we set up a new plasma discharge system to validate methods for investigating the magnetic structure in the lower atmosphere of the sun. The system successfully reproduced plasma parameters comparable to those of the solar prominence with helium discharge, and we observed spectropolarimetric signals from the anisotropic radiation and magnetic fields.

The Horizontal Spectrograph has a capability of simultaneous measurements of multiple wavelength windows with a high spectral resolution. As a future work, with helps of various plasma measurements such as probes and laser induced florescence, this system allows us to develop diagnostics methods for the three dimensional solar atmosphere under a weak magnetic field by multi-line measurement to resolve quantum interference among sublevels, e.g. the differential Hanle effect [37].

Acknowledgments

The research was supported by NIFS-DPS21 and the NIFS Collaboration Research Program NIFS22KIIH002.

[1] J.-F. Donati and J.D. Landstreet, Annu. Rev. Astron. Astrophys. **47**, 333 (2009).
[2] T. Chatani *et al.*, Sci. Rep. **12**, 15567 (2022).
[3] D.H. Mackay *et al.*, Space Sci. Rev. **151**, 333 (2010).
[4] N. Labrosse *et al.*, Space Sci. Rev. **151**, 243 (2010).
[5] A.A. van Ballegooijen and P.C.H. Martens, Astrophys. J. **343**, 971 (1989).
[6] D.M. Rust and A. Kumar, Sol. Phys. **155**, 69 (1994).
[7] D. Orozco Suárez *et al.*, Astron. Astrophys. **566**, A46 (2014).
[8] Y. Hanaoka and T. Sakurai, Astrophys. J. **851**, 130 (2017).
[9] J. Trujillo Bueno *et al.*, Nature **415**, 403 (2002).
[10] Y. Nakai and A. Hattori, Memoirs Faculty of Sciences University of Kyoto **36**, 385 (1985). URL http://hdl.handle.net/2433/257590
[11] K. Ichimoto *et al.*, Technical Reports from Astronomical Observatory, Graduate School of Science, Kyoto University **6**, 3 (2022). URL http://hdl.handle.net/2433/278127
[12] A. Kramida and NIST ASD Team (2022), NIST Atomic Spectra Database (ver. 5.10), [Online]. URL https://physics.nist.gov/asd [2017, April 9]. National Institute of Standards and Technology, Gaithersburg, MD.
[13] S. Kajita *et al.*, Phys. Plasmas **24**, 073301 (2017).
[14] N. Baguer *et al.*, J. Appl. Phys. **93**, 47 (2003).
[15] K.L. Bell *et al.*, J. Phys. B **1**, 18 (1968).
[16] S. Nowak *et al.*, Appl. Phys. B: Lasers Opt. **63**, 203 (1996).
[17] J. Trujillo Bueno and A. Asensio Ramos, Astrophys. J. **655**, 642 (2007).
[18] T. Fujimoto, J. Quant. Spectrosc. Radiat. Transfer **14**, 377 (1974).
[19] M. Goto, J. Quant. Spectrosc. Radiat. Transfer **76**, 331 (2003).
[20] A. Asensio Ramos *et al.*, Astrophys. J. **683**, 542 (2008).
[21] Y. Iida *et al.*, Phys. Plasmas **17**, 123301 (2010).
[22] T. Shikama *et al.*, J. Phys. D **49**, 025206 (2015).
[23] J. Hopwood, Plasma Sources Sci. Technol. **1**, 109 (1992).
[24] S. Parenti, Living Rev. Sol. **11**, 1 (2014).
[25] M. Hagino *et al.*, Society of Photo-Optical Instrumentation Engineers (SPIE) Conference Series **9151**, 91515V (2014).
[26] R. Tokuda *et al.*, Technical Reports from Astronomical Observatory, Graduate School of Science, Kyoto University **4**, 1 (2019). URL http://hdl.handle.net/2433/241382
[27] G. Ruan *et al.*, Astrophys. J. **865**, 123 (2018).
[28] D. Yamasaki *et al.*, accepted by Publ. Astron. Soc. Jpn.
[29] M. Goto, *Plasma Polarization Spectroscopy* (Springer Berlin, Heidelberg 2008) chap. 2.
[30] R.J. Rutten, *Radiative Transfer in Stellar Atmospheres* (Lecture Notes Utrecht University 2003) URL https://robrutten.nl/Radiative Transfer.html
[31] C.B. Markwardt, Astronomical Society of the Pacific Conference Series **411**, 251 (2009).
[32] J.J. Moré, *Lecture Notes in Mathematics*, vol. 630 (Springer, Berlin, Heidelberg 1978) p. 105.
[33] J.J. Moré and S.J. Wright, *Optimization Software Guide*

(Society for Industrial and Applied Mathematics 1993)
[34] W.E. Baylis, *Progress in Atomic Spectroscopy, part A* (1978) p. 1227.
[35] T. Fujimoto and S.A. Kazantsev, Plasma Phys. Control. Fusion **39**, 1267 (1997).
[36] R. Manso Sainz *et al.*, Astrophys. J. **788**, 118 (2014).
[37] J. Trujillo Bueno *et al.*, Astrophys. J. Lett. **746**, L9 (2012).